JACS
JOURNAL OF THE AMERICAN CHEMICAL SOCIETY
Article
pubs.acs.org/JACS

Morphological and Dimensional Control via Hierarchical Assembly of Doped Oligoaniline Single Crystals

Yue Wang,[†] Jinglin Liu,[‡] Henry D. Tran,[†] Matthew Mecklenburg,[§,⊥] Xin N. Guan,[†] Adam Z. Stieg,[⊥,∥] B. C. Regan,[§,⊥] David C. Martin,[‡] and Richard B. Kaner*[,†,⊥]

[†]Department of Chemistry and Biochemistry, University of California, Los Angeles, Los Angeles, California 90095-1969, United States

[‡]Department of Materials Science and Engineering, University of Delaware, Newark, Delaware 19716-1501, United States

[§]Department of Physics and Astronomy, University of California, Los Angeles, California 90095-1547, United States

[⊥]California NanoSystems Institute, Los Angeles, California 90095, United States

[∥]WPI Center for Materials Nanoarchitectonics, National Institute for Materials Science, Tsukuba, Ibaraki 305-0040, Japan

Supporting Information

ABSTRACT: Single crystals of doped aniline oligomers are produced via a simple solution-based self-assembly method. Detailed mechanistic studies reveal that crystals of different morphologies and dimensions can be produced by a "bottom-up" hierarchical assembly where structures such as one-dimensional (1-D) nanofibers can be aggregated into higher order architectures. A large variety of crystalline nanostructures including 1-D nanofibers and nanowires, 2-D nanoribbons and nanosheets, 3-D nanoplates, stacked sheets, nanoflowers, porous networks, hollow spheres, and twisted coils can be obtained by controlling the nucleation of the crystals and the non-covalent interactions between the doped oligomers. These nanoscale crystals exhibit enhanced conductivity compared to their bulk counterparts as well as interesting structure–property relationships such as shape-dependent crystallinity. Furthermore, the morphology and dimension of these structures can be largely rationalized and predicted by monitoring molecule–solvent interactions via absorption studies. Using doped tetraaniline as a model system, the results and strategies presented here provide insight into the general scheme of shape and size control for organic materials.

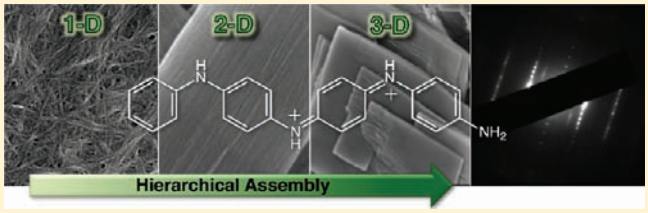

INTRODUCTION

Conducting organic molecular and polymeric materials are promising candidates for a variety of applications including organic photovoltaics, light-emitting diodes, field-effect transistors, gas sensors, memory devices, and stretchable electrodes.[1−7] Compared to many of their inorganic counterparts, organic conductors are advantageous in terms of their improved solution processability, facile and scalable synthesis, and the ability to tune their chemical and physical properties via molecular design.[8−12] However, the performance and stability of devices are largely governed by the ordering of molecules in solid state.[13,14] Hence, the device performance for organic conductors is often inferior as compared to their inorganic counterparts due to the lack of molecular order at the macroscopic level.[15,16] This is especially true for polymeric conductors such as polyaniline; as a result, the growth of single-crystalline organic conductors has become a highly desirable and rapidly evolving field of research.[13,17,18]

Crystals possessing nanoscale morphologies are of particular interest as they facilitate anisotropic carrier transport, serve as model systems for elucidating intrinsic transport properties and structure–property relationships, and help address the role of nanoscale domains in micro- and macrostructures.[13,16] However, crystallizing conducting polymers such as polyaniline has been extremely challenging due to the free energy and kinetic barriers associated with inducing polymer chains to rearrange from their preferred coiled conformations to an ordered crystalline state.[19−22] Therefore, in order to achieve higher crystallinity, low-molecular-weight polyaniline or oligomers of aniline are the preferred choice because they resemble small molecules in regard to crystallization kinetics.[23,24] In particular, doped oligoanilines serve as a unique middle ground between polyaniline and molecular conductors since they retain most properties of the parent polymer, while their monodispersed molecular chains can be processed into more ordered states and have the potential to achieve precise ordering in crystalline domains or layers that can lead to high carrier mobility and conductivity—properties typically associated with small-molecule conductors.[15,25,26]

Despite their advantages, reports on doped oligoanilines are sparse, and most previous studies in this field have focused on the synthesis of these molecules or their use as model systems for probing the properties of polyaniline.[27−31] Recently, we reported a solution-based self-assembly method for growing nanostructures for a variety of doped aniline oligomers.[24] By

Received: February 1, 2012
Published: May 25, 2012

   dx.doi.org/10.1021/ja301061a | J. Am. Chem. Soc. 2012, 134, 9251−9262

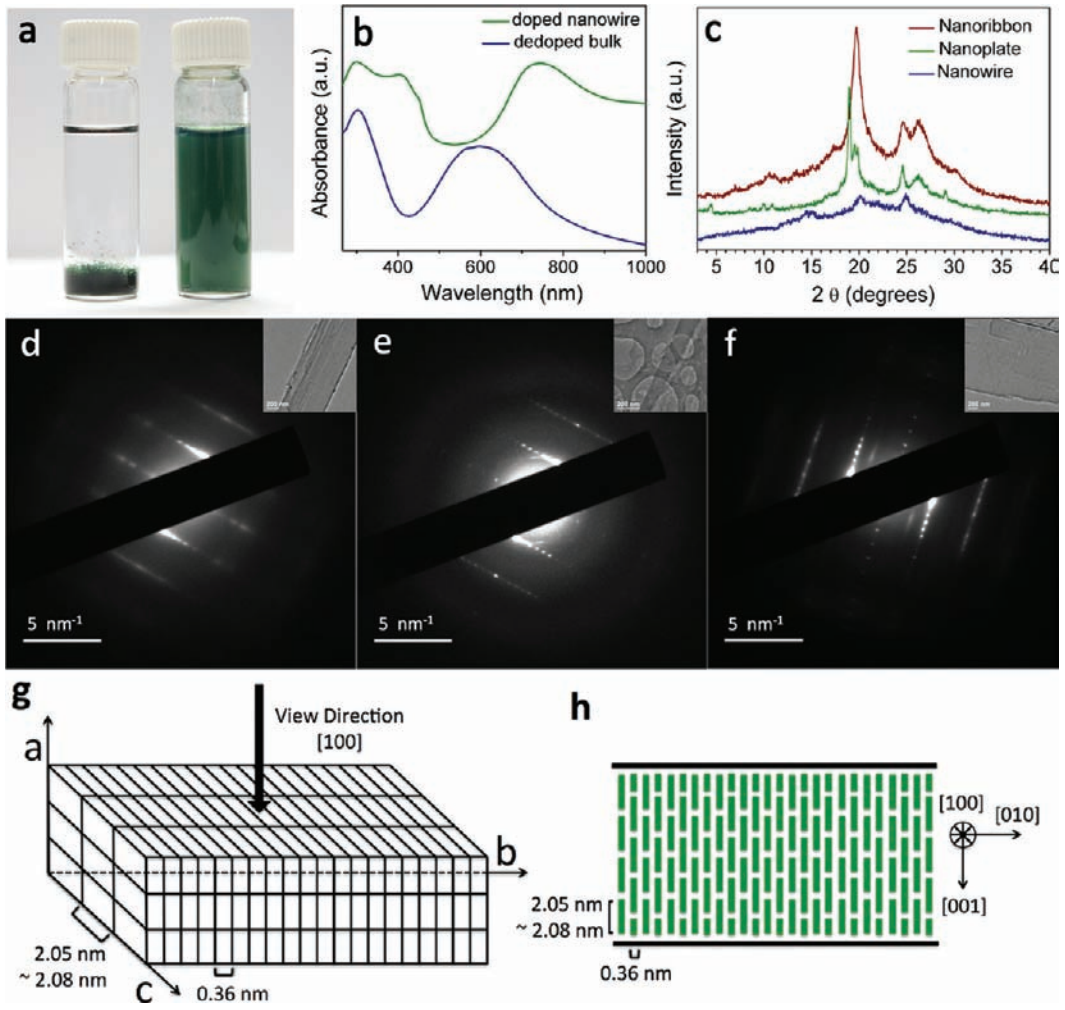

Figure 1. (a) Photographs showing the cotton-like state of tetraaniline nanowires in water (left) and the homogeneous dispersion formed upon agitation (right). (b) UV–vis spectra of the dedoped bulk powder prior to self-assembly and the final doped nanowires dispersed in water. (c) XRD patterns for tetraaniline nanowires, nanoribbons, and nanoplates. (d–f) SAED patterns for the nanowires (d), nanoribbons (e), and nanoplates (f). The insets show the corresponding bright-field TEM images for each structure. (g) A 3-D packing model of tetraaniline with the corresponding *d*-spacings in the *b*- and *c*-directions. (h) A 2-D packing model illustrated as a projection in the [100] direction for the nanoribbon and nanoplate samples. The green rectangles represent the tetraaniline molecules.

exploiting the interplay between various non-covalent interactions including hydrogen bonding, $\pi-\pi$ stacking, and hydrophobic and electrostatic interactions, four different shapes were obtained: nanowires, nanoribbons, nanoplates, and nanoflowers. The resulting nanostructures show enhanced crystallinity and conductivity compared to their bulk counterparts based on previous reports.[24]

Here, we demonstrate that *single crystals* of *electroactive*, *doped* phenyl/amine-capped tetraaniline (hereafter referred to as tetraaniline), the smallest repeat unit that can represent polyaniline in its conductive emeraldine salt oxidation state, can be grown from such a self-assembly process. Reports on single crystals of oligoanilines are exceedingly rare and have only focused on structural analysis.[29,32,33] We show that the ordered solid-state packing of our doped oligomers leads to a 2-order-of-magnitude increase in their conductivity compared to the highest value from previous reports.[28,31] Furthermore, we thoroughly investigate the morphological evolution of these crystals at various assembly intervals in order to elucidate the effect of each driving force on the self-assembly process. The nanofiber structure, which appears to be a readily attainable morphology for organic conductors such as polyaniline and their derivatives,[8] can be transformed into a large array of higher dimensional nanocrystals with a variety of sizes and shapes by creating a suitable self-assembly environment. With a clearer understanding of this "bottom-up" hierarchical assembly mechanism, we demonstrate the ability to exquisitely tune the crystal's supramolecular architecture from 1-D nanofibers and nanowires to 2-D ribbons, sheets, and plates, and eventually 3-D flower-like structures, hollow spheres, porous sheets, and twisted ropes. Moreover, due to the unique acid–base doping–dedoping properties of oligomers and polymers of aniline, the electrostatic interactions introduced by the dopants can serve conveniently as one of the driving forces for self-assembly. During this process, the dopants are simultaneously incorporated producing tetraaniline crystals in their conductive emeraldine salt oxidation state. The sizes of many of these structures can be fine-tuned simply by controlling the degree of aggregation dictated by pH.

dx.doi.org/10.1021/ja301061a | *J. Am. Chem. Soc.* 2012, 134, 9251–9262

EXPERIMENTAL SECTION

Synthesis. *N*-Phenyl-1,4-phenylenediamine was purchased from Sigma-Aldrich and used without further purification. Amine/phenyl-capped tetraaniline was synthesized via a previously reported route.[34] In short, iron(III) chloride was mixed with stoichiometric amounts of *N*-phenyl-1,4-phenylenediamine in 0.1 M HCl with vigorous stirring for 2 h. The suspension was then filtered and washed repeatedly with water and acetone. The product was subsequently dedoped using 0.1 M ammonium hydroxide and recrystallized from ethanol three times. Phenyl/phenyl-capped tetraaniline was synthesized by a modified condensation reaction in an inert atmosphere via a published method.[35] In brief, the phenyl/amine-capped tetraaniline starting material in the reported reaction was replaced by a stoichiometric amount of *N*-phenyl-1,4-phenylenediamine. Characterization of these products can be found in refs 24 and 34.

Self-Assembly of Nanostructures. In a typical process, 2.0 mg of finely powdered oligoaniline was added to a solvent mixture of 1.0 mL of an organic solvent and 4.0 mL of an aqueous acidic solvent at room temperature. The resulting mixture was briefly swirled and left undisturbed for 4−5 days. At the end of the self-assembly process, the mixture was purified by dialysis against deionized water. The product was collected after approximately 1 day. For time-lapsed experiments, the water bath was stirred and replaced with fresh water continually to accelerate the dialysis process; the final product was collected after approximately 5 h.

Microscopy. Scanning electron microscopy (SEM) and transmission electron microscopy (TEM) samples were prepared by drop-casting an oligoaniline dispersion onto a piece of silicon wafer and a TEM grid, respectively. All SEM images were acquired on a JEOL JSM-6700 field emission scanning electron microscope. The TEM images shown in Figures 2 and 4 were obtained with a FEI/PHILIPS CM 120 transmission electron microscope operated at an accelerating voltage of 120 kV.

The low-dose electron diffraction patterns and corresponding bright-field images in Figure 1 were taken with a JEOL JEM-2010F FasTEM instrument at 200 kV accelerating voltage. *d*-spacings on electron diffraction patterns were calibrated using polycrystalline gold films and analyzed using ImageJ (National Institutes of Health) software. The samples were observed to be beam sensitive. During in situ observations of the electron beam-induced changes of the diffraction patterns, we found that the Bragg reflections transformed from sharp localized spots to streaks in the [001] direction at characteristic doses ranging from 0.02 to 0.07 C/cm^2. With extended exposure to the beam, scattering faded completely.

The selected area electron diffraction (SAED) patterns (Supporting Information, Figure S4) and the corresponding bright-field images were collected on a FEI Tecnai G^2 TF20 transmission electron microscopy at 200 kV accelerating voltage.

Atomic force microscopy (AFM) images were acquired in the dynamic mode (AM-AFM) on a Nanoscope V Dimension Icon instrument (Bruker AXS) under ambient conditions using phosphorus n$^+$-doped silicon cantilevers (PPP-NCST, Nanosensors) with a nominal spring constant of 7.4 N/m, first longitudinal resonance frequencies between 130 and 165 kHz, and a nominal tip radius of <10 nm. Simultaneous height and phase images were acquired and reproduced from multiple samples. Simple plane fitting of the acquired images enabled subsequent cross-sectional analyses. The reported values exhibited no significant variation between different samples or cantilever probes (see Supporting Information).

Other Characterization Techniques. Powder X-ray diffraction (PXRD) patterns were obtained on a Panalytical X'Pert Pro X-ray powder diffractometer using a Cu Kα radiation beam with a wavelength of 0.15418 nm. The diffractometer was operated at 45 kV and 40 mA at a scan rate of 4.0° /min, with an angular 2θ range from 3 to 40°. UV−vis spectra were acquired on a HP 8452 spectrometer.

RESULTS AND DISCUSSION

As-synthesized tetraaniline in its emeraldine base oxidation state lacks a well-defined structure and exhibits only granular features.[24,34] However, nanostructures of tetraaniline can be obtained by a post-synthetic self-assembly process in which a small amount of tetraaniline is placed in a solvent mixture that involves a good solvent such as ethanol and a poor solvent such as aqueous 0.1 M HCl, to promote the molecule−molecule interactions that are essential for forming crystalline structures.[24,36] A number of nanostructures can be induced just by varying the dopant acid: HCl, HNO_3, $HClO_4$, and H_2SO_4. These acids can lead to nanowires, nanoribbons, nanoplates, and flower-like structures, respectively. The products can readily be dispersed in water (Figure 1a), which allows convenient solution-based processing methods such as drop-casting or spray-coating. UV−vis spectra confirm that the final nanostructures are in the emeraldine salt oxidation state with characteristic absorption maxima at 290, 405, and 735 nm (Figure 1b). These values can be contrasted with the starting bulk material in the emeraldine base oxidation state with absorption peaks at 295 and 585 nm (Figure 1b).[37] PXRD indicates that these doped structures are significantly more crystalline than typical nanostructures of polyaniline (Figure 1c), which is in agreement with the fact that low-molecular-weight oligomers can more readily pack into ordered architectures.

Crystal Structures. SAED is a powerful tool for characterizing the structure of nanosized domains and understanding the associated structure−property relationships for materials.[38] Low-dose TEM techniques are employed here to collect SAED patterns for tetraaniline nanowires, nanoribbons, and nanoplates (Figure 1d−f) in order to minimize the possible beam damage to the samples.

The electron diffraction patterns show that all three tetraaniline morphologies are single crystals. The sharp spots in the diffraction patterns confirm a high degree of crystallinity and large crystallites, while streaking in certain characteristic directions indicates the existence of planar defects. The diffraction patterns share a predominant *d*-spacing of ∼0.36 nm in the direction along the long axes of the crystals, defined as *b* (Figure 1g). This *d*-spacing is confirmed by the presence of a ∼24.6° 2θ peak in the XRD patterns shared by all three samples (Figure 1c). Nanoribbons and nanoplates show large *d*-spacings of ∼2.08 and ∼2.05 nm, respectively, in the direction defined as *c* (Figure 1g). Similar large *d*-spacings are also expected for the nanowire sample, but strong streaking in the *c*-direction due to packing disorder between these planes prevents us from acquiring accurate values. The results also indicate a tendency for the crystals to orient with the (100) planes parallel to the substrate, allowing the normal viewing direction to be [100], as illustrated in Figure 1g. The angles between [001] and [010] are measured to be 90°, and the patterns seem to be nearly (but not always exactly) mirror symmetric.

Comparison of the SAED patterns with the corresponding bright-field TEM images, shown as insets of Figure 1d−f, clearly suggests that the long axes of the crystals are always oriented along the [010] direction. Strong scattering along [010] indicates that the molecules are nominally perpendicular to this direction, i.e., perpendicular to the long axis of the crystal. For nanoribbons and nanoplates, there are systematic odd absences on the (00*l*) planes, consistent with glide

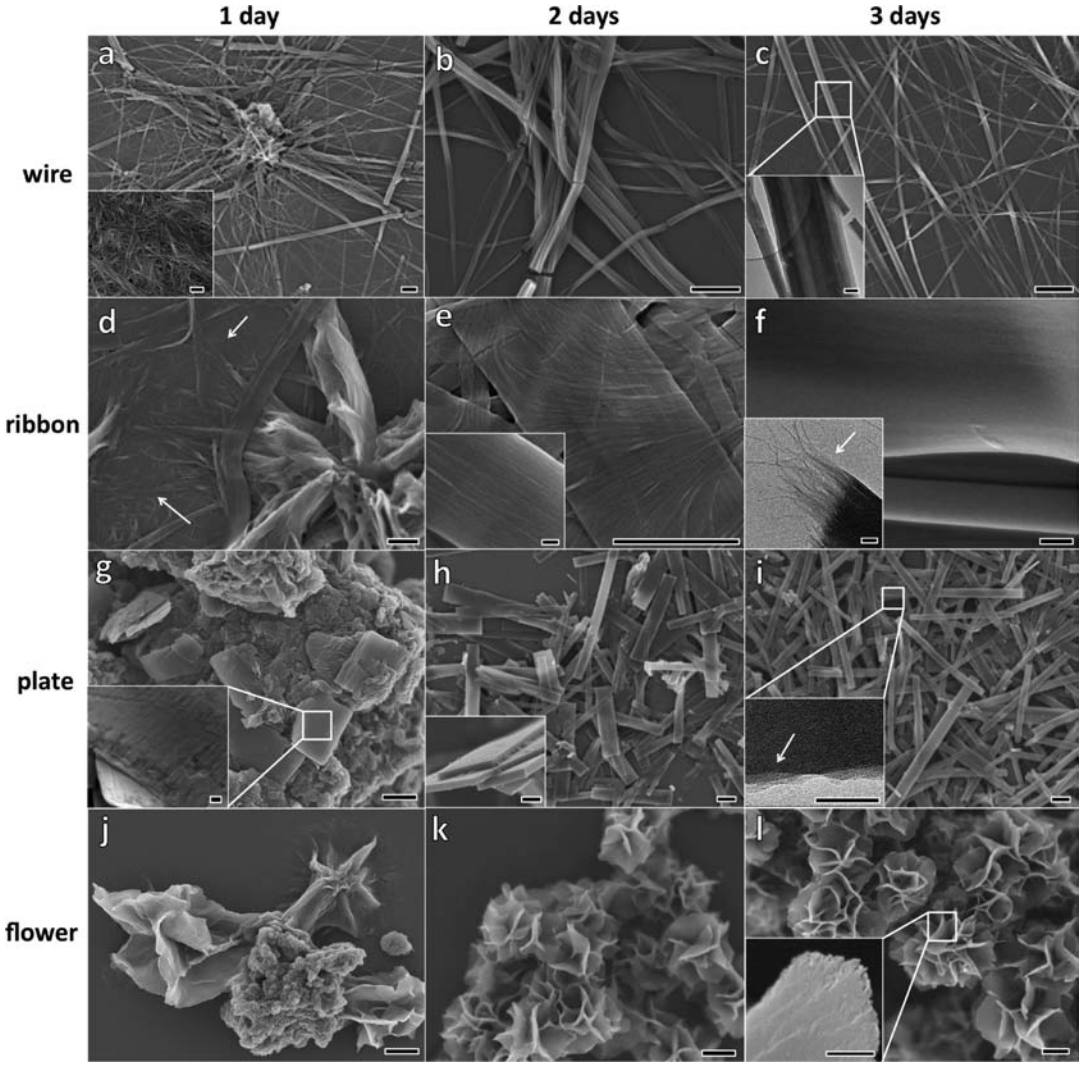

Figure 2. Evolution of tetraaniline crystals. SEM images showing nanowires (a–c), nanoribbons (d–f), nanoplates (g–i), and nanoflowers (j–l) collected after 1, 2, and 3 days of assembly. Insets: (a) the thin nanofibers during the early stages of nanowire formation, (c) a TEM image of a single wire, (e) a magnified view of a ribbon exhibiting clear nanofiber fringes on the surface, (f) a TEM image revealing the oriented fiber-like structures at one end of a ribbon. Insets in (g), (h), and (i) show a zoom-in on the surface of an initial plate, a tilted cross-sectional view, and the edge of a plate observed via TEM, respectively. The inset in (l) illustrates the layered-structure of a single "petal". Scale bars: (a)–(e), (g)–(l), and inset of (l) = 1 μm; (f) and all other insets = 100 nm.

symmetry and therefore indicative of a possible alternating packing arrangement, as shown in Figure 1h. Interestingly, highly streaked diffuse diffraction intensity can also be observed for the nanoplates at intermediate scattering positions between (000) and (010) at one-third (weaker) and two-thirds (stronger) spacings.

The high degree of order in the diffraction patterns suggests that the conformation of the tetraaniline molecules is consistent and regular. SAED patterns collected at various tilt angles have shown their 3-D solid-state structure to be highly crystalline as well. Experiments are currently underway to decipher the complete packing arrangements of these crystals.

The few previous reports on single crystals of oligoanilines have only provided structural information.[29,32,33] Here we demonstrate that the high molecular packing order of our crystals manifests itself in a significant increase in conductivity when comparing the crystals to conventional doped bulk tetramer.[24] Two-probe $I-V$ measurements via bottom-contact devices for a single nanowire, nanoribbon, or nanoplate reveal their conductivities to be as high as 0.3, 1.1, and 0.5 S/cm along the b-axis, respectively (Figure S1 and Table S1). Although conductivity values for the highly crystalline nanoribbons and nanoplates with sharp SAED spots are slightly higher than those of the less crystalline nanowires with highly streaked SAED patterns, they are on the same order of magnitude despite theoretical prediction of a more significant difference.[17] This can be attributed to the bottom-contact configuration of the electrodes, where contact quality tends to vary from device to device. However, when comparing these single crystals to bulk doped tetraaniline, particularly the nanoribbons (1.1 S/cm), their conductivity is 2 orders of magnitude higher than the highest previously reported values, and is on the same order of magnitude as conventional, doped, unprocessed polyaniline, whose molecular chain is hundreds of units longer.[28,39]

Crystal Evolution. Time-lapsed mechanistic studies were carried out to monitor the evolution of the nanoscale morphologies produced for tetraniline. When the process is quenched via rapid dialysis after 1 day of growth, nucleation

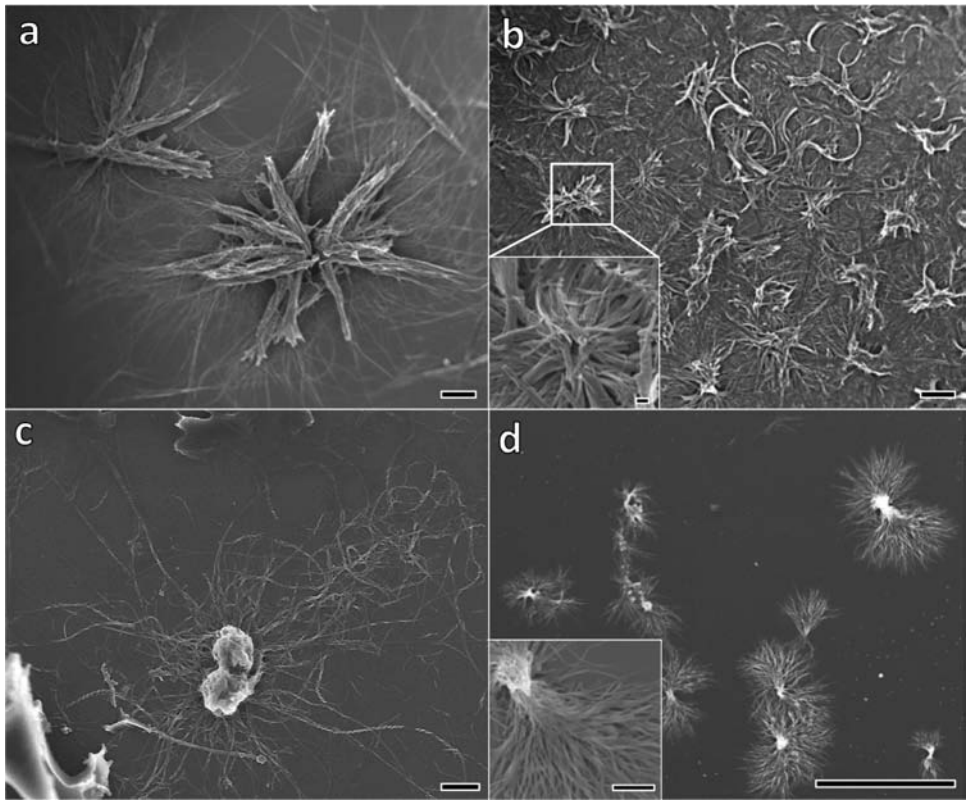

Figure 3. Distinctive nucleation centers are visible in diluted areas for various oligomers: (a) tetraaniline nanowires, (b) tetraaniline nanoribbons, (c) dianiline nanofibers, and (d) phenyl-capped tetraaniline nanofibers. Scale bars: (a), (b), and (d) = 10 μm; (c) and the insets in (b) and (d) = 1 μm.

centers and small nanofeatures are found when doped with HCl or HNO_3. For HCl-doped tetraaniline, directionally elongated nucleation centers comprised of aggregated, rigid wires are observed (Figure 2a), while HNO_3-doped ones form clusters of sheets/ribbons as nucleation centers (Figure 2d). In fact, such nucleation centers can still be seen in diluted areas of the final product after 5 days of assembly (Figure 3a,b). Increased magnification of these samples reveals that large amounts of nascent nanofibers with diameters of ~10 nm also exist at this stage of the crystallization process (Figure 2a, inset, and areas highlighted by arrows in Figure 2d). However, after 2 days of growth, most of the thin nanofibers either transform into thicker and more rigid fibers when doped with HCl (Figure 2b) or orient parallel to each other and merge into nanoribbons that have a significantly larger width than thickness with HNO_3 as the dopant. After 3 days, high aspect ratio crystalline nanowires with diameters of ~100−400 nm and lengths of hundreds of micrometers were formed throughout the HCl-doped sample (Figure 2c). While the nanowire surfaces appear to be smooth in the SEM images, TEM analysis of an individual wire reveals its genesis in multiple thinner nanofibers (Figure 2c, inset). The fibrillar origin of the higher order structures can be more readily observed in the HNO_3-doped ribbons. Figure 2e shows a bundle of parallel-oriented small nanofibers prior to forming a defined ribbon structure, while the inset to Figure 2e illustrates a mature ribbon with clear surface fringes that have dimensions similar to those of the pristine nanofibers. The surface of most nanoribbons smoothes out after 3 days (Figure 2f). However, a TEM image (Figure 2f, inset) of the terminus of a nanoribbon clearly shows its nanofibrillar origin. The genesis of nanofibers for both nanowires and nanoribbons is further confirmed by AFM analyses shown in Figures S2 and S3.

Unlike the nanowire and nanoribbon samples, $HClO_4$-doped nanoplates nucleate off of the surface of bulk agglomerates (Figure 2g). A magnified view of a pristine plate (Figure 2g, inset) illustrates its layered structure. Within each layer, aligned arrays of small nanofibers similar to those in the ribbon sample are also observed. Plates with well-defined features are formed after 2 days (Figure 2h). Further maturing appears to increase the yield and aspect ratio of the plates, indicating that the growth rate along the (010) facet is the fastest (Figure 2i). Although the surfaces of these plates appear to be smooth under SEM, a magnified view of the edge of a plate under TEM (Figure 2i, inset) as well as the height profile extracted from AFM analyses (Figures S2 and S3) reveals their pristine layered structure, which suggests that the plates originate from merged stacks of sheets.

Tetraaniline doped with H_2SO_4 follows a pattern similar to that of the nanoplates in which the flower-like structures nucleate off of the agglomerates. Small clusters of randomly oriented sheets can be observed after 1 day of self-assembly (Figure 2j). The clusters accumulate more sheets (or "petals") and evolve into flower-like structures after an additional day (Figure 2k). Further growth appears to increase the yield but does not appear to change the size of the nanoflowers (Figure 2l). A magnified view of a single "petal" (Figure 2l, inset) demonstrates that the layered structure within these petal-like sheets is responsible for the flowers.

These time-lapsed experiments provide a visualization of how the crystallization process evolves for tetraaniline nanostructures and suggest a two-step formation mechanism: (1) nucleation and (2) growth by hierarchical assembly. Dedoped

dx.doi.org/10.1021/ja301061a | J. Am. Chem. Soc. 2012, 134, 9251−9262

Scheme 1. Illustration of the "Bottom-Up" Hierarchical Assembly Mechanism Believed Responsible for the Formation of Oligoaniline Crystals with Different Shapes and Dimensions[a]

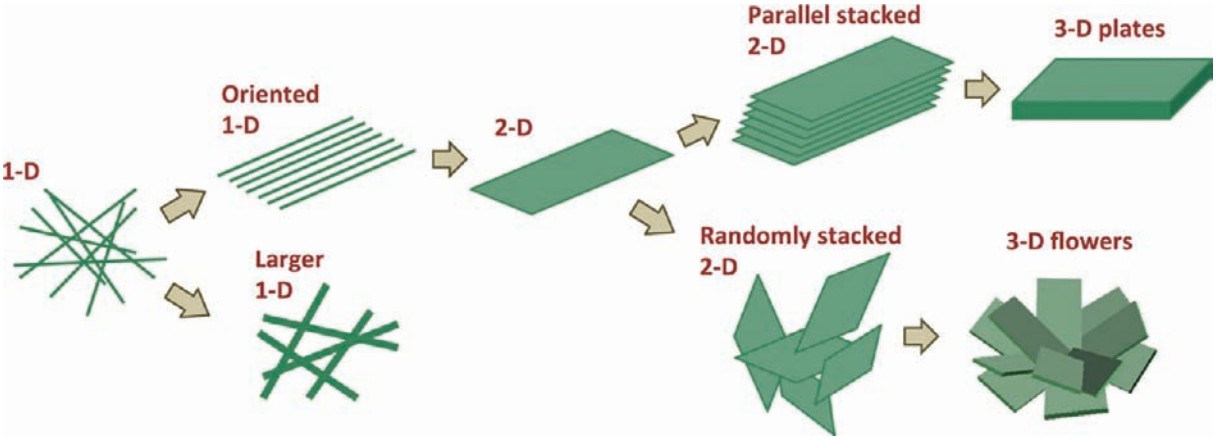

[a]The small features such as 1-D nanofibers (diameter <10 nm) either aggregate into more rigid 1-D nanowires or orient parallel to each other to form 2-D ribbons. The 2-D sheets can further stack in an orderly fashion leading to rigid 3-D plates, or stack randomly yielding a 3-D flower-like morphology.

tetraaniline, in its emeraldine base oxidation state, is soluble in common organic solvents such as ethanol. While insoluble in acidic aqueous solvents, tetraaniline can be doped into the conducting emeraldine salt state in such an environment. A 1:4 (v/v) ethanol:acidic aqueous solvent ratio is typically used in this self-assembly process. The 20% concentration of ethanol is sufficient to solvate dedoped tetraaniline molecules. However, once doped into the emeraldine salt by the acids from the aqueous phase, tetraaniline becomes insoluble in both ethanol and water. Local supersaturation is then quickly reached, and clusters of doped tetraaniline molecules precipitate out, forming nucleation centers in the solution.

The morphology of the nucleation centers appears to dictate the final tetraaniline crystal superstructure. For example, rigid rod-like nucleation centers that elongate directionally (Figure 2a or 3a) lead to high-aspect ratio nanowires, while ribbon-like clusters result in the formation of nanoribbons (Figure 2d or 3b). In fact, similar phenomena are also observed in other oligoaniline systems; for instance, using the same process, dianiline nanofibers often grow from clusters of very thin and short nanofibers (Figure 3c), while phenyl/phenyl-capped tetraaniline nanofibers/nanowires form from dendrite-like nucleation centers (Figure 3d). Such observations and conclusions are not surprising, as the nanoscale size and shape tuning for many inorganic (semi)conductors are achieved partially by controlling the morphology of the nucleation centers.[40] Comparable nucleation centers have also been observed for some small-molecule conductors[36] and biomolecules.[41]

Once well-defined nucleation centers are present, the nanostructures appear to form through a merging mechanism, where structures with smaller feature sizes, such as nanofibers, merge into larger architectures such as nanowires when doped with HCl or nanoribbons when doped with HNO_3. Based on the evolution of the crystal morphologies, a hierarchical assembly mechanism is proposed (Scheme 1). First, small 1-D nanoscale features such as thin nanofibers form during the initial stages of self-assembly along with the nucleation centers. Such small crystals with low stacking order are often the kinetic products of crystallization and tend to form quickly in large quantities.[40,42] Next, with increasing growth time the randomly oriented thin nanofibers either merge onto the thicker nanowires extending from the nucleation centers (e.g., when doped with HCl) to form larger and more rigid 1-D nanowires or orient parallel to the (001) facet of the larger ribbons around the nucleation centers (e.g., when doped with HNO_3) to form ribbon- or sheet-like 2-D structures. Subsequently, the 2-D ribbons or sheets can further preferentially attach onto their (100) surface, leading to plate-like architectures with well-defined 3-D dimensions. Alternatively, an apparently random stacking organization, possibly due to twin crystallization,[43,44] can result in an as-grown flower-like morphology. Further evidence for hierarchical assembly comes from AFM measurements on the crystals found with fringes on their surfaces (Figures S2 and S3). AFM phase images (Figure S2d–f) as well as high-resolution cross-sectional analyses (Figure S3) clearly show that both nanowires and nanoribbons are comprised of small, characteristic features that are ~7.5 nm in diameter, which also corresponds to the vertical step height along the edge of a typical nanoplate (see Supporting Information for a more detailed discussion). The driving force for the maturing of the smaller morphologies into higher order structures is likely the minimization of surface free energy of a system within a given volume to transform the kinetic product into a more thermodynamically favorable one, analogous to the Ostwald ripening process. Similar mechanisms have been observed for various other systems including inorganic crystals, biomolecules, and carbon-based materials.[42,45−48] This ripening process also renders higher order crystals to be more ordered, evident from the sharp diffraction spots manifested by ribbons or plates (Figure 1e,f) as opposed to the streaked SAED patterns for the 1-D nanowires (Figure 1d). Distinct self-assembly environments are created when different protonic acids are used to dope the tetraaniline, which leads to different types of electrostatic interactions between the positively charged backbone and the counter-anion. Hence, the transformation of smaller features into higher order architectures terminates at different stages of the hierarchical assembly timeline for each system.

Controlling Crystal Morphology and Dimensionality. Non-covalent interactions including $\pi-\pi$ stacking, hydrophobic interactions, and hydrogen-bonding are key elements for the

dx.doi.org/10.1021/ja301061a | J. Am. Chem. Soc. 2012, 134, 9251−9262

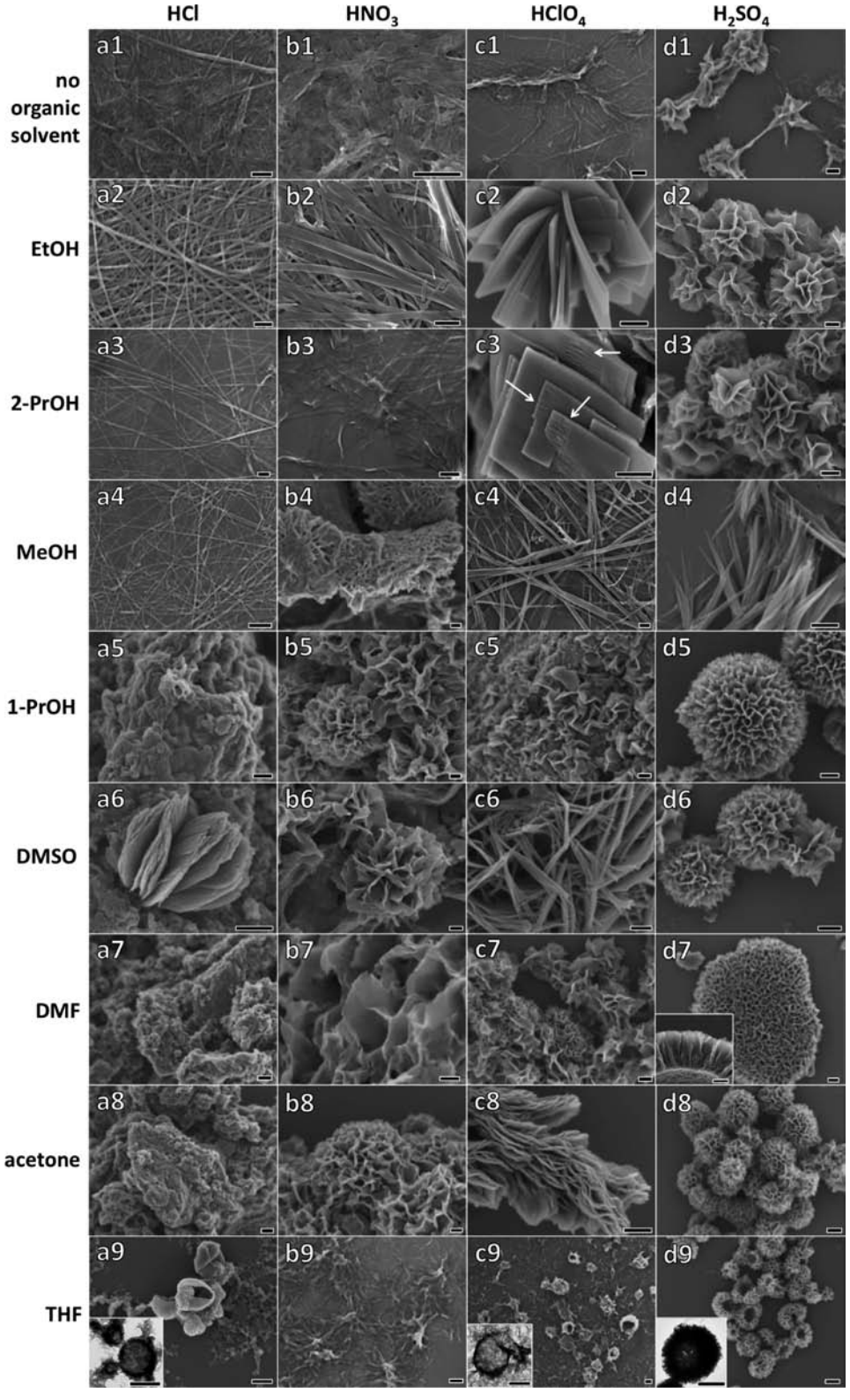

Figure 4. Extensive control over the morphology of the tetraaniline crystals can be achieved by creating distinct self-assembly environments using different combinations of the doping acids, HCl, HNO_3, $HClO_4$, and H_2SO_4 (as indicated at the top) with eight different organic solvents (as indicated along the left side). The SEM images of the structures formed using these different dopants and organic solvents are shown here along with an aqueous control (a1−d1) shown at the top. Inset in d7 shows the cross section of the porous sheet. Insets in a9, c9, and d9 are the corresponding TEM images illustrating the nanostructures' hollow nature. Scale bars = 1 μm.

self-assembly of many organic (semi)conductors and biomolecules. Controlling solvent conditions such as polarity and the ability to form hydrogen bonds serves as a convenient method for tuning molecule−molecule and solvent−molecule interactions, which in turn determine the intermolecular aggregation that ultimately dictates supramolecular struc-

dx.doi.org/10.1021/ja301061a | J. Am. Chem. Soc. 2012, 134, 9251−9262

tures.[13,18,49,50] Here, we strive to gain an understanding of (1) how each applicable non-covalent interaction:$\pi-\pi$ stacking and hydrophobic interactions induced by solvent mixtures, and the electrostatic interactions aroused from molecule−dopant interactions, shapes the morphology of tetraaniline and (2) how the variation of pH allows for further tuning of the sizes of each morphology.

In order to study the non-covalent interactions controlled by the organic solvent leading to doped tetraaniline nanostructures, we maintain a constant electrostatic interaction factor, i.e., by using the same protonic doping acid. For example, all tetraaniline morphologies shown in Figure 4a1−a9 are assembled from the same aqueous component (0.1 M HCl) but using different organic solvents. On the other hand, the solvent is kept constant going across a row in Figure 4; for example, panels a2, b2, c2, and d2 are produced under an identical solvent environment (ethanol and water) but are subject to different electrostatic interactions (i.e., different doping acids).

Organic solvents clearly play an important role in tuning the self-assembly conditions. Note that without any organic solvents in the system, only poorly defined structures can be obtained (Figure 4a1, b1, c1, and d1). Weak arcs and rings are observed on their corresponding SAED patterns (Figure S4), suggesting these morphologies are semi-crystalline with preferential packing orientation. Hence, electrostatic interactions alone do not appear sufficient to shape doped tetraaniline into single-crystalline structures. Only the lower order morphology on the hierarchical assembly scheme (Scheme 1), i.e., nanofibers, can be formed in most cases. However, when different organic solvents are used, distinct morphologies across all stages of hierarchical assembly can be produced for tetraaniline doped with the same acid, which is evident by examining each column in Figure 4. Using the $HClO_4$-doped tetraaniline systems as examples (Figure 4c1−c9), rigid and well-defined nanoplates are the preferred morphology when ethanol or 2-propanol is used. However, 1-D nanowires are obtained by simply changing the organic phase to methanol or DMSO. Loosely stacked 2-D sheets form in the presence of acetone, while 1-propanol, DMF, and THF lead to 3-D superstructures such as randomly stacked sheets, flowers, and hollow spheres, respectively. Note that the plates in Figure 4c3 also clearly reveal their origin, as a layered 2-D sheet architecture comprised of oriented arrays of 1-D nanofibers (highlighted by arrows) can be observed, further supporting the proposed hierarchical assembly mechanism (Scheme 1).

To understand why a small amount of an organic solvent can have such a profound effect on the morphology, we dissolved the dedoped tetraaniline in its emeraldine base oxidation state in each of the eight different organic solvents used in Figure 4 in order to monitor molecule-solvent interactions via absorption spectra. A solvatochromism effect is observed in the combined, normalized UV−vis plot as shown in Figure 5. The peaks around 300 nm can be assigned to the $\pi-\pi^*$ transition.[37] Tetraaniline dissolved in short-chain alcohols including ethanol, 2-propanol, methanol, and 1-propanol has a $\pi-\pi^*$ transition at around 310 nm. DMSO and DMF cause this peak to red shift to 325 nm, while acetone and THF further moves the transition to higher wavelengths of ca. 328 and 340 nm, respectively. The red shift of this absorption peak is often attributed to weaker intermolecular interactions as a more distorted $\pi-\pi$ stacking makes lower energy excitonic transitions allowable.[51−53] To directly observe the effect of organic

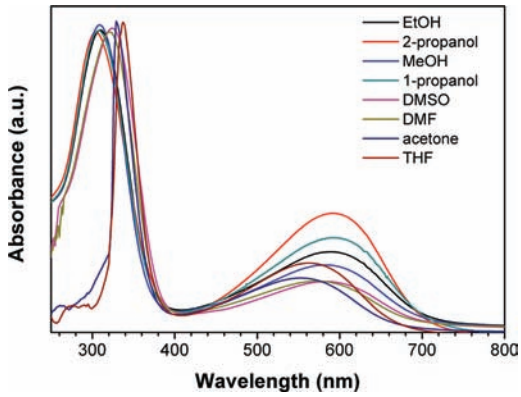

Figure 5. Normalized UV−vis spectra of tetraaniline in its emeraldine base oxidation state dissolved in the eight organic solvents (0.167 mg/mL) used to produce morphologies in Figure 4. The solvatochromism observed here indicates that tetraaniline molecules aggregate differently in these organic solvents: (a) ethanol, (b) 2-propanol, (c) methanol, (d) 1-propanol, (e) dimethyl sulfoxide (DMSO), (f) dimethylformamide (DMF), (g) acetone, and (h) tetrahydrofuran (THF).

solvents on the aggregation of molecules, dedoped tetraaniline was dried out from each of these solvents. The resulting solid morphologies are shown in Figure S5. Well-defined architectures such as nanospheres were obtained for tetraaniline dried from the alcohols in most cases (Figure S5a−d), indicating stronger intermolecular aggregation in agreement with the conclusion from UV−vis spectroscopy. On the other hand, the solvents leading to higher wavelength $\pi-\pi^*$ absorptions yield agglomerates without any defined structures in most cases (Figure S5e−h), suggesting weaker intermolecular interactions, consistent with the evidence provided by the UV−vis spectra. Observed peaks at ∼580 nm are responsible for the π-to-polaron band transition,[37] and their positions also vary depending on the solvent. In short-chain alcohols such as ethanol, 2-proponal, and methanol, this transition appears around 590 nm, while for acetone or THF the transition occurs around 560 nm. The onset of the peaks at longer wavelength suggests a lower π-to-polaron band transition energy, which corresponds to a more extended chain conformation that often leads to higher crystallinity and enhanced conductivity.[21,37,54] Furthermore, the effect of the organic solvent obtained from the absorption spectra coincides with the SEM observations, as solvents that result in better $\pi-\pi$ stacking and more extended chain conformations, such as ethanol, 2-propanol, and methanol, tend to result in more ordered and better-defined nanostructures (Figure 4). On the other hand, distinctively different morphologies can be obtained with organic solvents that lead to almost identical UV−vis absorptions, e.g., ethanol vs methanol, 2-propanol vs 1-propanol. Solvent molecules can be incorporated as part of the crystal structures in solution-based crystallization processes, including oligoaniline- and polyaniline-based systems, which could have a considerable effect on the crystal morphology and packing arrangement.[29,42,43,55] It is possible that despite the similar interactions between these solvents and the tetraaniline molecules in solution, the small amount of solvent molecules trapped in the tetraaniline crystals plays a significant role in directing their final morphologies due to their different sizes, properties, and interactions with the adjacent tetraaniline molecules. The

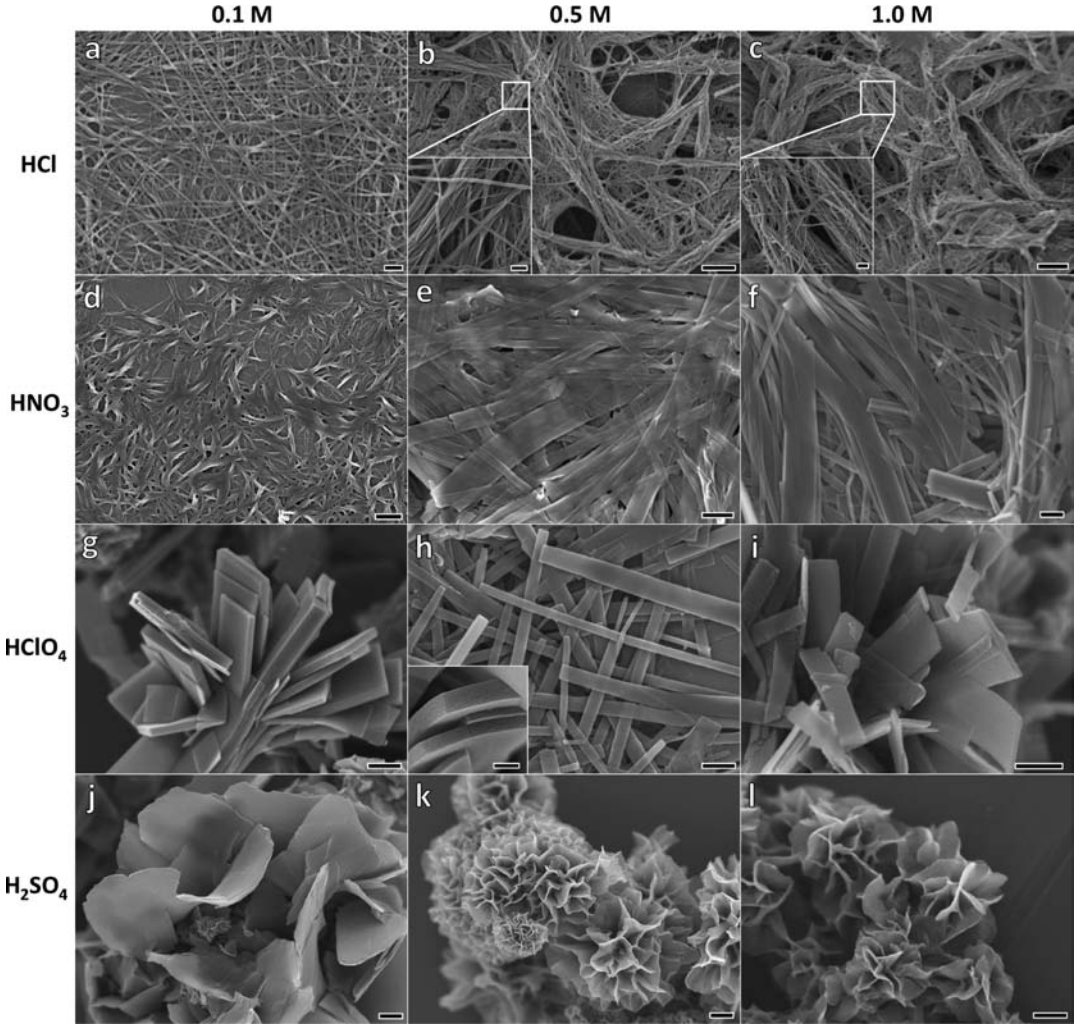

Figure 6. In addition to controlling the crystal morphology, the feature size of each of the nanostructures can be further tuned by varying the solvent acidity. The SEM images show the different sizes of the HCl-doped nanowires (a–c), the HNO_3-doped nanoribbons (d–f), the $HClO_4$-doped nanoplates (g–i), and the H_2SO_4-doped nanoflowers (j–l) obtained using acid concentrations of 0.1, 0.5, and 1.0 M, respectively. Scale bars: (a), (d)–(l), and insets of (b) and (c) = 1 μm; (b) and (c) = 10 μm; inset of (h) = 100 nm.

detailed packing structure and the number of solvent molecules per unit cell are currently under investigation.

In addition, a preferred morphology is often associated with certain organic solvents. For example, methanol leads to 1-D wire/fiber structures regardless of the doping acid (Figure 4a4, b4, c4, d4). Various forms of stacked sheets, mostly nanoflowers, can be obtained when using 1-propanol, DMF, or acetone, while different hollow structures including hollow spheres or hollow flowers tend to form when THF is chosen as the organic phase. Such observations suggest that the organic solvent molecules could have a structural guiding effect by interacting, and possibly forming complexes or participating in solid-state packing with the tetraaniline molecules during self-assembly to shape their aggregates into a particular morphology. Similar solvent templating behavior has been observed in other molecular systems.[56−58]

Different electrostatic interactions created by using selected protonic dopant acids when the organic solvent conditions are kept constant results in additional variation in morphologies, as seen by examining a row in Figure 4, e.g., compare panels a2, b2, c2, and d2. Therefore, by combining electrostatic interactions provided by the dopants with hydrophobic and $\pi-\pi$ interactions created using different organic solvents, a large library of nanostructures of various shapes and dimensions can be achieved from the hierarchical assembly (Figure 4). Additionally, complex structures such as twisted coils (Figure S6) are possible by varying other parameters, e.g. the self-assembly temperature. Such extensive morphological control has been hitherto difficult to achieve for organic materials.

Furthermore, the sizes of these nanocrystals can be readily tuned by taking advantage of the unique intermolecular electrostatic repulsion properties of oligo/polyaniline. For example, nanowires are the preferred morphology to form in the HCl/ethanol solvent system. When 0.1 M HCl is used, individual nanowires are well dispersed in solution (Figure 6a). However, when the acid concentration is increased to 0.5 or 1.0 M, bundles of nanowires are typically obtained (Figure 6b,c and insets). Similar effects are observed for the HNO_3/ethanol (Figure 6d–f) and the H_2SO_4/ethanol (Figure 6j–l) systems, as lower acid concentration leads to smaller or less aggregated structures, while increased acidity results in larger or more aggregated architectures. Interestingly, an inverse trend is observed for the $HClO_4$/ethanol system, as stacks of thicker nanoplates (thickness ~100–500 nm) form when a low concentration, 0.1 M $HClO_4$ solution is used (Figure 6g). As the acid concentration increases to 0.5 and 1.0 M, well-

dx.doi.org/10.1021/ja301061a | J. Am. Chem. Soc. 2012, 134, 9251–9262

dispersed individual plates and thin, somewhat flexible plates become the preferred morphology, respectively (Figure 6h,i).

Such pH-dependent crystal size control arises from the positive charges on the molecular chains of oligomers (e.g., tetraaniline) or polymers of aniline when in their emeraldine salt oxidation state and doped with a protonic acid. The positive charges result in electrostatic repulsion between the doped tetraaniline molecules. When the tetraaniline backbone is fully protonated, the maximum number of positive charges is obtained, leading to a strong intermolecular repulsion.[21,54] Hence, discrete morphologies, such as individual, well-separated nanowires (in 0.1 M HCl/ethanol), short and fiber-like ribbons (in 0.1 M HNO_3/ethanol), or micrometer-sized sheets (in 0.1 M H_2SO_4/ethanol) form as a smaller number of molecules aggregate to form crystals. Excess protonic acid, i.e., when using a higher acid concentration, serves as islands of neutralization agents for the positive charges on the tetraaniline backbone.[54] This screening effect shields the positively charged tetraaniline molecules from each other and thus decreases the repulsive forces between molecules.[54,59] Therefore, a greater number of doped tetraaniline molecules can aggregate to form architectures that are larger in size, such as thicker and more rigid nanoribbons (in 1 M HNO_3/ethanol), or bundles of nanostructures, such as nanowire bundles (in 1 M HCl/ethanol) and nanoflowers with many sheets/"petals" (in 1 M H_2SO_4/ethanol). On the other hand, when tetraaniline molecules are not fully protonated, an insufficient amount of positive charge may not exert sufficient repulsion to keep the smaller features separated. Hence, nanostructures with larger sizes (i.e., thicker plates) can be obtained. This may help explain the inverted trend in the $HClO_4$/ethanol system in which lower acid concentration yields larger and more rigid structures. The variance in trend with each acid system could be caused by the different types of electrostatic interactions associated with the different doping acids.

Structure–Property Relationships. Choosing the $HClO_4$-doped system as an example, we attempted to quantify the crystallinity of the tetraaniline nanostructures produced with different organic solvents using PXRD (Figure 7). The three most dominant peaks in all diffraction patterns (19.1, 24.6, and 26.3° 2θ) remain at the same positions for all morphologies. The most intense peak at 19.1° 2θ corresponds to a d-spacing of 0.46 nm, which is the intermolecular packing distance with the dopant anion ClO_4^- incorporated between adjacent chains.[24,33,55] The peak at ~24.6° 2θ corresponds to the d-spacing of ~0.36 nm along the b-axis, as shown in Figure 1h. A π–π stacking distance of ~0.34 nm can be calculated from the peak at 26.3° 2θ and is typically observed in well-ordered organic conducting crystals.[9,55] When short-chain alcohols such as ethanol, 2-propanol, methanol, or 1-propanol are used as the organic solvent, the resulting nanostructures exhibit well-defined peaks with high intensity at these three 2θ positions (Figure 7a–d). DMSO, DMF, and acetone (Figure 7e–g) lead to morphologies that show broader and less intense peaks at these positions. The least crystalline structure with very weak diffraction patterns occurs when THF is used (Figure 7h). The crystallinity, as quantified by XRD, is in good agreement with the direct observations from the SEM images in Figure 4, as ethanol and 2-propanol lead to well-defined nanoplates with sharp edges, which is an indication of higher crystallinity, while the hollow spheres grown from the THF/$HClO_{4(aq)}$ mixture appear to be less ordered in nature.

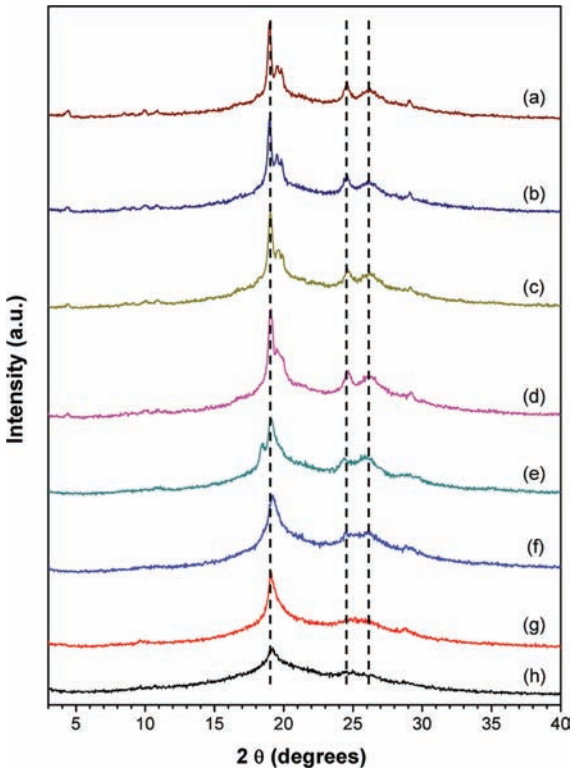

Figure 7. Powder X-ray diffraction patterns indicate that the different shapes of tetraaniline crystals doped with $HClO_4$ but assembled using (a) ethanol, (b) 2-propanol, (c) methanol, (d) 1-propanol, (e) DMSO, (f) DMF, (g) acetone, and (h) THF (Figure 4c2–c9) possess the same 2θ positions for the three most intense characteristic peaks, but different levels of crystallinity and variations in some other peaks.

In addition to the three dominant, characteristic peaks, several peaks including those at ~4.4, 8.5, 10.0, 10.9, 19.6, and 29.1° 2θ appear with increasing nanostructure crystallinity, while others such as the ~18.5° 2θ peak in Figure 7e cannot be observed in other spectra. Therefore, it is likely that these morphologies obtained with the same dopant yet different organic solvents share a similar crystal structure, but with some variation in packing arrangement. Detailed structural analysis is currently under investigation.

■ CONCLUSIONS

We have demonstrated that single crystals of doped tetraaniline with different shapes and sizes can be produced through a simple self-assembly process. Detailed mechanistic studies and microscopic analyses suggest that simple features such as 1-D nanofibers can aggregate into higher order architectures such as 2-D nanoribbons or 3-D nanoplates. Further morphological and dimensional control is readily achieved by tuning (1) the shape of the nucleation centers and (2) the non-covalent interactions including electrostatic, hydrophobic, and π–π interactions. Monitoring interactions between the dedoped tetraaniline and the organic solvent via absorption studies can assist in the selection of a suitable organic phase for achieving a preferred morphology or crystallinity. The sizes of the crystals can be further tuned by controlling the degree of aggregation. The library of doped crystalline tetraaniline nanostructures reported here can serve as a basis for extensive structure–property relationship investigations. With inorganic conductors, this type of information has enabled many structure-dependent

dx.doi.org/10.1021/ja301061a | J. Am. Chem. Soc. 2012, 134, 9251–9262

applications, including catalysis and plasmonic enhancement,[40] but it has been difficult to achieve with their organic counterparts partly due to the challenge in generating a large variety of supramolecular structures. We have established a correlation between the crystallinity of the oligoaniline crystals with their morphologies and dimensions in this report and are currently examining other structure−property relationships.

■ ASSOCIATED CONTENT

Supporting Information

Molecular structures of the oligoanilines, conductivity comparisons, AFM studies, additional SAED and SEM images. This material is available free of charge via the Internet at http://pubs.acs.org.

■ AUTHOR INFORMATION

Corresponding Author

kaner@chem.ucla.edu

Notes

The authors declare no competing financial interest.

■ ACKNOWLEDGMENTS

We thank Dr. Yongquan Qu for help with some of the TEM imaging and Dr. Chaoying Ni, Director of the W. M. Keck Electron Microscopy Laboratory at the University of Delaware, for help obtaining and calibrating the selected area diffraction patterns. We also acknowledge the use of the Nano and Pico Characterization Lab at the California NanoSystems Institute for AFM analysis. Support for this work has been provided by the UCLA based Focused Center Research Program Functional Engineered NanoArchetectonics center (R.B.K.), the National Science Foundation Small Business Technology Transfer program under Award No. 1010540 (H.D.T. and R.B.K.), the National Science Foundation through the Division of Materials Research (DMR-1103027) (D.C.M.), and a National Science Foundation Graduate Research Fellowship (Y.W.).

■ REFERENCES

(1) Briseno, A. L.; Mannsfeld, S. C. B.; Ling, M. M.; Liu, S.; Tseng, R. J.; Reese, C.; Roberts, M. E.; Yang, Y.; Wudl, F.; Bao, Z. N. *Nature* **2006**, *444*, 913.
(2) Chen, H. Y.; Hou, J.; Zhang, S.; Liang, Y.; Yang, G.; Yang, Y.; Yu, L.; Wu, Y.; Li, G. *Nat. Photonics* **2009**, *3*, 649.
(3) Lipomi, D. J.; Tee, B. C. K.; Vosgueritchian, M.; Bao, Z. N. *Adv. Mater.* **2011**, *23*, 1771.
(4) Sasabe, H.; Takamatsu, J.; Motoyama, T.; Watanabe, S.; Wagenblast, G.; Langer, N.; Molt, O.; Fuchs, E.; Lennartz, C.; Kido, J. *Adv. Mater.* **2010**, *22*, 5003.
(5) Virji, S.; Huang, J. X.; Kaner, R. B.; Weiller, B. H. *Nano Lett.* **2004**, *4*, 491.
(6) Tseng, R. J.; Huang, J. X.; Ouyang, J.; Kaner, R. B.; Yang, Y. *Nano Lett.* **2005**, *5*, 1077.
(7) Kim, F. S.; Ren, G. Q.; Jenekhe, S. A. *Chem. Mater.* **2011**, *23*, 682.
(8) Tran, H. D.; Li, D.; Kaner, R. B. *Adv. Mater.* **2009**, *21*, 1487.
(9) Anthony, J. E. *Chem. Rev.* **2006**, *106*, 5028.
(10) Liang, Y. Y.; Yu, L. P. *Acc. Chem. Res.* **2010**, *43*, 1227.
(11) Li, D.; Huang, J. X.; Kaner, R. B. *Acc. Chem. Res.* **2009**, *42*, 135.
(12) Lloyd, M.; Anthony, J.; Malliaras, G. *Mater. Today* **2007**, *10*, 34.
(13) Lim, J. A.; Liu, F.; Ferdous, S.; Muthukumar, M.; Briseno, A. L. *Mater. Today* **2010**, *13*, 14.
(14) Zhang, Y. J.; Dong, H. L.; Tang, Q. X.; Ferdous, S.; Liu, F.; Mannsfeld, S. C. B.; Hu, W. P.; Briseno, A. L. *J. Am. Chem. Soc.* **2010**, *132*, 11580.
(15) Reese, C.; Bao, Z. *Mater. Today* **2007**, *10*, 20.
(16) Li, R. J.; Hu, W. P.; Liu, Y. Q.; Zhu, D. B. *Acc. Chem. Res.* **2010**, *43*, 529.
(17) Bredas, J. L.; Street, G. B. *Acc. Chem. Res.* **1985**, *18*, 309.
(18) Briseno, A. L.; Mannsfeld, S. C. B.; Jenekhe, S. A.; Bao, Z.; Xia, Y. *Mater. Today* **2008**, *11*, 38.
(19) Wang, Y.; Tran, H. D.; Kaner, R. B. *J. Phys. Chem. C* **2009**, *113*, 10346.
(20) Lee, K.; Cho, S.; Park, S. H.; Heeger, A. J.; Lee, C. W.; Lee, S. H. *Nature* **2006**, *441*, 65.
(21) MacDiarmid, A. G.; Epstein, A. J. *Synth. Met.* **1995**, *69*, 85.
(22) Yan, Y.; Wang, R.; Qiu, X. H.; Wei, Z. X. *J. Am. Chem. Soc.* **2010**, *132*, 12006.
(23) Di Maria, F.; Olivelli, P.; Gazzano, M.; Zanelli, A.; Biasiucci, M.; Gigli, G.; Gentili, D.; D'Angelo, P.; Cavallini, M.; Barbarella, G. *J. Am. Chem. Soc.* **2011**, *133*, 8654.
(24) Wang, Y.; Tran, H. D.; Liao, L.; Duan, X. F.; Kaner, R. B. *J. Am. Chem. Soc.* **2010**, *132*, 10365.
(25) MacDiarmid, A. G. *Synth. Met.* **1997**, *84*, 27.
(26) Zang, L.; Che, Y. K.; Moore, J. S. *Acc. Chem. Res.* **2008**, *41*, 1596.
(27) Udeh, C. U.; Fey, N.; Faul, C. F. J. *J. Mater. Chem.* **2011**, *21*, 18137.
(28) Wei, Z. X.; Faul, C. F. J. *Macromol. Rapid Commun.* **2008**, *29*, 280.
(29) Shacklette, L. W.; Wolf, J. F.; Gould, S.; Baughman, R. H. *J. Chem. Phys.* **1988**, *88*, 3955.
(30) Wang, Y.; Tran, H. D.; Kaner, R. B. *Macromol. Rapid Commun.* **2011**, *32*, 35.
(31) Surwade, S. P.; Agnihotra, S. R.; Dua, V.; Manohar, N.; Jain, S.; Ammu, S.; Manohar, S. K. *J. Am. Chem. Soc.* **2009**, *131*, 12528.
(32) Baughman, R. H.; Wolf, J. F.; Eckhardt, H.; Shacklette, L. W. *Synth. Met.* **1988**, *25*, 121.
(33) Zhou, Y. C.; Geng, J. X.; Li, G.; Zhou, E. L.; Chen, L.; Zhang, W. J. *J. Polym. Sci., Polym. Phys.* **2006**, *44*, 764.
(34) Zhang, W. J.; Feng, J.; MacDiarmid, A. G.; Epstein, A. J. *Synth. Met.* **1997**, *84*, 119.
(35) Lu, F. L.; Wudl, F.; Nowak, M.; Heeger, A. J. *J. Am. Chem. Soc.* **1986**, *108*, 8311.
(36) Che, Y. K.; Datar, A.; Balakrishnan, K.; Zang, L. *J. Am. Chem. Soc.* **2007**, *129*, 7234.
(37) Xia, Y. N.; Wiesinger, J. M.; Macdiarmid, A. G.; Epstein, A. J. *Chem. Mater.* **1995**, *7*, 443.
(38) Martin, D. C.; Chen, J. H.; Yang, J. Y.; Drummy, L. F.; Kubel, C. *J. Polym. Sci., Polym. Phys.* **2005**, *43*, 1749.
(39) Chandrasekhar, P. *Conducting Polymers, Fundamentals and Applications: A Practical Approach*; Kluwer Academic Publishers: Boston, 1999.
(40) Xia, Y. N.; Xiong, Y. J.; Lim, B.; Skrabalak, S. E. *Angew. Chem., Int. Ed.* **2009**, *48*, 60.
(41) Rimer, J. D.; An, Z.; Zhu, Z.; Lee, M. H.; Goldfarb, D. S.; Wesson, J. A.; Ward, M. D. *Science* **2010**, *330*, 337.
(42) Boistelle, R.; Astier, J. P. *J. Cryst. Growth* **1988**, *90*, 14.
(43) Geng, J. F.; Zhou, W. Z.; Skelton, P.; Yue, W. B.; Kinloch, I. A.; Windle, A. H.; Johnson, B. F. G. *J. Am. Chem. Soc.* **2008**, *130*, 2527.
(44) Sounart, T. L.; Liu, J.; Voigt, J. A.; Huo, M.; Spoerke, E. D.; McKenzie, B. *J. Am. Chem. Soc.* **2007**, *129*, 15786.
(45) Challa, S. R.; Delariva, A. T.; Hansen, T. W.; Helveg, S.; Sehested, J.; Hansen, P. L.; Garzon, F.; Datye, A. K. *J. Am. Chem. Soc.* **2011**, *133*, 20672.
(46) Pashuck, E. T.; Stupp, S. I. *J. Am. Chem. Soc.* **2010**, *132*, 8819.
(47) Ziserman, L.; Lee, H. Y.; Raghavan, S. R.; Mor, A.; Danino, D. *J. Am. Chem. Soc.* **2011**, *133*, 2511.
(48) Viculis, L. M.; Mack, J. J.; Kaner, R. B. *Science* **2003**, *299*, 1361.
(49) Briseno, A. L.; Mannsfeld, S. C. B.; Lu, X. M.; Xiong, Y. J.; Jenekhe, S. A.; Bao, Z. N.; Xia, Y. N. *Nano Lett.* **2007**, *7*, 668.
(50) Briseno, A. L.; Mannsfeld, S. C. B.; Reese, C.; Hancock, J. M.; Xiong, Y.; Jenekhe, S. A.; Bao, Z.; Xia, Y. N. *Nano Lett.* **2007**, *7*, 2847.
(51) Prasanthkumar, S.; Saeki, A.; Seki, S.; Ajayaghosh, A. *J. Am. Chem. Soc.* **2010**, *132*, 8866.

(52) Balakrishnan, K.; Datar, A.; Oitker, R.; Chen, H.; Zuo, J. M.; Zang, L. *J. Am. Chem. Soc.* **2005**, *127*, 10496.
(53) Wurthner, F. *Chem. Commun.* **2004**, 1564.
(54) MacDiarmid, A. G.; Epstein, A. J. *Synth. Met.* **1994**, *65*, 103.
(55) Winokur, M. J.; Mattes, B. R. *Macromolecules* **1998**, *31*, 8183.
(56) Balakrishnan, K.; Datar, A.; Naddo, T.; Huang, J. L.; Oitker, R.; Yen, M.; Zhao, J. C.; Zang, L. *J. Am. Chem. Soc.* **2006**, *128*, 7390.
(57) Wang, Y.; Dea, P. *J. Chem. Eng. Data* **2009**, *54*, 1447.
(58) Park, C.; Song, H. J.; Choi, H. C. *Chem. Commun.* **2009**, 4803.
(59) Li, D.; Kaner, R. B. *Chem. Commun.* **2005**, 3286.